Science Advances
AAAS

advances.sciencemag.org/cgi/content/full/5/10/eaax4769/DC1

Supplementary Materials for

Controlling three-dimensional optical fields via inverse Mie scattering

Alan Zhan*, Ricky Gibson, James Whitehead, Evan Smith, Joshua R. Hendrickson, Arka Majumdar*

*Corresponding author. Email: azhan137@gmail.com (A.Z.); arka@uw.edu (A.M.)

Published 4 October 2019, *Sci. Adv.* **5**, eaax4769 (2019)
DOI: 10.1126/sciadv.aax4769

This PDF file includes:

Section S1. The GMMT and specification of FOM

We here briefly describe the algorithm and formulation of the inverse design problem. We begin by specifying both the wavelength of interest and an initial condition of scatterers including their refractive index, positions, and initial radii. At each iteration, the forward problem is solved for a distribution of spheres in order to calculate the figure of merit (FOM). Then, the inverse problem is solved to obtain a gradient to provide an update direction for the radius distribution. The forward problem is solved using GMMT and is described fully elsewhere (*28–30*). The initial and scattered fields in spherical coordinates in terms of spherical vector wave function (SVWF) multipoles are expressed as

$$\boldsymbol{E}_{init}(\boldsymbol{r}_j) = \sum_{i,n} a^i_{in,n} \boldsymbol{\psi}^{(1)}_n(\boldsymbol{r}_i - \boldsymbol{r}_j) \text{ (1a)}$$
$$\boldsymbol{E}_{scat}(\boldsymbol{r}_j) = \sum_{i,n} b^i_n \boldsymbol{\psi}^{(3)}_n(\boldsymbol{r}_i - \boldsymbol{r}_j) \text{ (1b)}$$

where $b^{i'}_{n'}$ is the scattering coefficient of a spherical wave corresponding to multipole n', originating at the center of sphere i', $a^{i'}_{n',in}$ is a coefficient corresponding to the spherical wave of mulitpole n' comprising the initial wave incident on sphere i', and $\boldsymbol{\psi}^{(1)}_n$ ($\boldsymbol{\psi}^{(3)}_n$) are the incoming (outgoing) SVWFs. For a system of i = 1… N spheres described by a multipole expansion with super index n = 1 … n_{max} (including the orbital index l, azimuthal index m, and polarization index p), the relationship between the initial and scattered coefficients is described by an equation of the form

$$M^{i\,i'}_{n\,n'} b^{i'}_{n'} = T^{i\,i'}_{n\,n'} a^{i'}_{n',in} \text{ (2)}$$

where T is a block diagonal matrix with diagonals populated by each scatterer's individual scattering matrix or T-matrix. In the special case of spheres, each individual T-matrix is diagonal, so T itself is diagonal. M is the system scattering matrix and is defined as

$$M^{i\,i'}_{n\,n'} = \delta_{i\,i'}\delta_{n\,n'} - T^{i\,i''}_{n\,n''} W^{i''\,i'}_{n''\,n'} \text{ (3)}$$

where the δ matrices are Kronecker delta functions, T is the same matrix as previously defined, and W is a coupling matrix describing the contribution of the scattered field of sphere i' on the incident field of sphere i. The elements of the W matrix are populated by the SVWF translation addition operators and contain all position information relevant to the sphere ensemble. In this way, GMMT naturally separates the material and geometric properties of the individual scatterers from their positions.

The figure of merit is a sum of squared error defined as

$$FOM(\boldsymbol{R}) = \sum_j \left(I_0(\boldsymbol{r}_j) - I_k(\boldsymbol{r}_j, \boldsymbol{R})\right)^2 \text{ (4)}$$

where I_k is the intensity profile generated by the current iteration of the device with a sphere radius distribution $\boldsymbol{R}$, and I_0 is the desired intensity profile. For both devices, we

define our desired intensity profile I_0 as 22 different points; 8 points describe the positions where intensity is chosen to be a nonzero value (20), while the other 14 points are regularization points where the intensity is chosen to be zero. In fig. S1, the points in blue are chosen to be zero while the points in yellow are chosen to be nonzero.

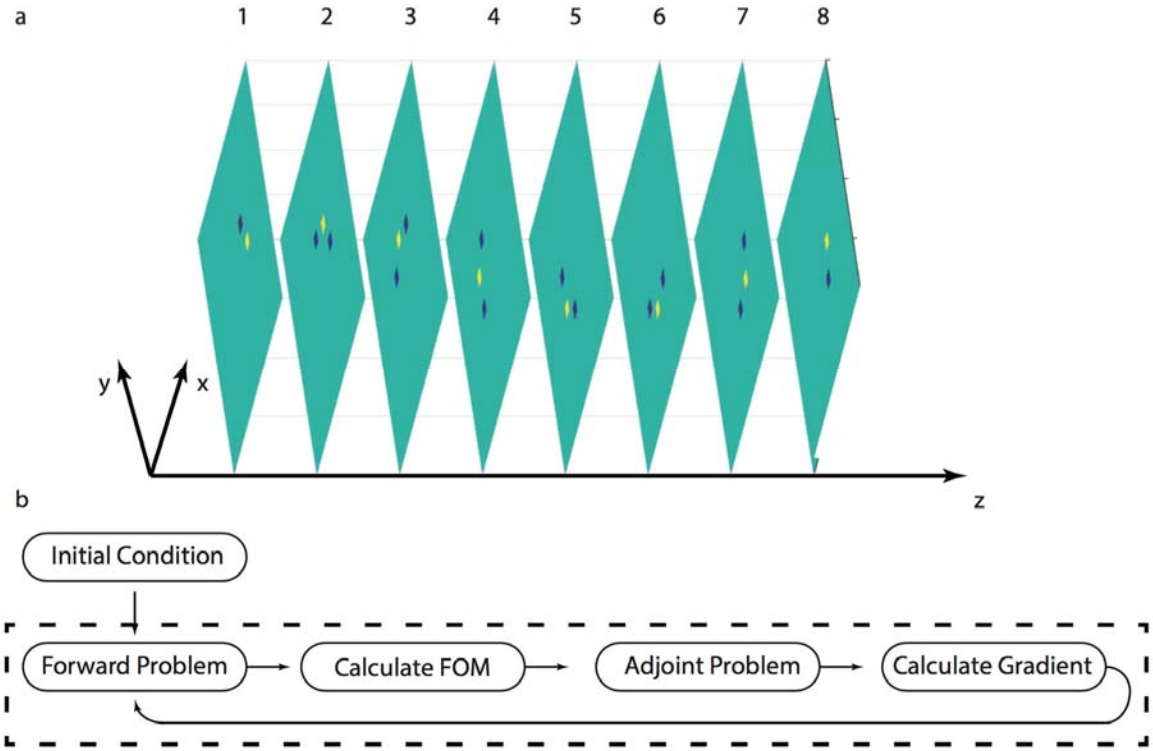

Fig. S1. Optimization scheme. (**a**) Specification of the figure of merit showing the discrete helix form. The yellow points denote places where the helix is specified and the blue points denote places where the intensity is minimized. The helix is specified on 8 transverse planes along the optical (z) axis. (**b**) Optimization steps showing the general progression of the algorithm. The steps in the dashed box are completed in a single iteration.

Using the adjoint method, we can construct the gradient of our specified FOM in terms of the radii of our given sphere configuration. A derivation of the gradient of the FOM is given in the supplementary material S2. The key benefit of using the adjoint method is known to be the ease in which the gradient is computed. Instead of computing each partial derivative separately and solving a system of equations for each, we can compute all of them using parameters obtained from solving a single system of equations.
With this gradient information, we use LBFGS-B, a well-known quasi-Newton method to optimize our FOM (*41*). The specific implementation is rewritten in C and run from a Matlab wrapper (*42*). The optimization scheme is shown in Figure 1b, where the steps in the dashed box constitute a single iteration.

Table S1. Benefits and drawbacks of the design approach.

Pros	Cons
1. Fully analytic model not requiring any meshing of a finite volume. (No perfect matched layers or complicated boundary conditions required). 2. Rigorous computation of electric fields in all space. 3. Rigorous modeling of coupling between scatterers and does not rely on local phase approximation. 4. Memory scaling with number of scatterers rather than spatial dimension. 5. Capable of specifying fully three-dimensional optical field distributions. 6. Robust block diagonal preconditioner for solving large linear system of equations.	1. Limited scatterer geometry in current spherical implementation. 2. Does not account for substrate effects.

Section S2. Derivation of the derivative

We would like to construct a gradient of a given desired figure of merit (FOM) with respect to a given set of variables. In the specific case described in our manuscript, with our figure of merit defined as (4), we would like to take the gradient of the squared error between an iterate intensity distribution I_k and a desired intensity distribution I_0 with respect to the sphere radii $\boldsymbol{R}$ that compose the optical element. Using the chain rule, we express a constituent partial derivative with respect to a single sphere radius as

$$\frac{\partial FOM}{\partial R_l} = 2\,Re\left\{\frac{\partial FOM}{\partial \boldsymbol{b}} \cdot \frac{\partial \boldsymbol{b}}{\partial R_l}\right\} \quad (5)$$

where $\boldsymbol{b}$ is a vector containing the scattered field coefficients (b_n^i) obtained by solving the forward generalized multisphere Mie theory (GMMT) scattering problem

$$M_{n\,n'}^{i\,i'}(\boldsymbol{R}) b_{n'}^{i'}(\boldsymbol{R}) = T_{n\,n'}^{i\,i'}(\boldsymbol{R}) a_{n',in}^{i'} \quad (6)$$

with

$$M_{n\,n'}^{i\,i'}(\boldsymbol{R}) = \delta_{i\,i'}\delta_{n\,n'} - T_{n\,n''}^{i\,i''}(\boldsymbol{R}) W_{n''n'}^{i''\,i'} \quad (7)$$

now showing terms with an explicit dependence on the sphere radii. The first term in (5), readily calculated as the figure of merit, is specified as an analytical function of the scattering coefficients $\boldsymbol{b}$, and for a specific coefficient b_n^i, it is given by

$$\frac{\partial FOM}{\partial b_n^i} = -2\sum_j \left(I_0(\boldsymbol{r}_j) - I_k(\boldsymbol{r}_j)\right) \boldsymbol{E}^*(r_j) \cdot \boldsymbol{\psi}_n^{(3)}(\boldsymbol{r}_j - \boldsymbol{r}_i) \quad (8)$$

where $\boldsymbol{E}^*$ is the complex conjugate of the electric field, and $\boldsymbol{\psi}_n^{(3)}$ is the outgoing SVWFs. The second term in (5) is generally the more computationally expensive term, and the main benefit of the adjoint method lies in avoiding explicitly computing $\frac{\partial \boldsymbol{b}}{\partial R_l}$. Explicitly the derivative with respect a single sphere radius R_l is given by

$$\frac{\partial \boldsymbol{b}_{\boldsymbol{n}}^{\boldsymbol{i}'}}{\partial R_l} = \left(M_{n\,n'}^{i\,i'}\right)^{-1}\left(\frac{\partial T_{n\,n'}^{i\,i'}}{\partial R_l} a_{n',in}^{i'} + \frac{\partial T_{n\,n''}^{i\,i''}}{\partial R_l} W_{n''n'}^{i''\,i'} b_{n'}^{i'}\right) \quad (9)$$

where we have taken a derivative of (6) with respect to R_l and isolated the relevant derivative. Then, rather than solving (9), we can directly substitute it into (5) to arrive at

$$\frac{\partial FOM}{\partial R_l} = 2\,Re\left\{\frac{\partial FOM}{\partial b_{n'}^{i'}}\left(M_{n\,n'}^{i\,i'}\right)^{-1}\left(\frac{\partial T_{n\,n'}^{i\,i'}}{\partial R_l} a_{n',in}^{i'} + \frac{\partial T_{n\,n''}^{i\,i''}}{\partial R_l} W_{n''n'}^{i''\,i'} b_{n'}^{i'}\right)\right\} \quad (10)$$

We can define a new set of 'adjoint' coefficients λ_n^i with the first two terms in the derivative defined as

$$\left(\lambda_n^i\right)^T = \frac{\partial FOM}{\partial b_{n'}^{i'}}\left(M_{n\,n'}^{i\,i'}\right)^{-1} \quad (11)$$

and construct an 'adjoint' system of equations

$$\left(M_{n\,n'}^{i\,i'}\right)^T \lambda_n^i = \left(\frac{\partial FOM}{\partial b_{n'}^{i'}}\right)^T \quad (12)$$

Substituting in (11) into (10), we obtain

$$\frac{\partial FOM}{\partial R_l} = 2\,Re\left\{\left(\lambda_n^i\right)^T\left(\frac{\partial T_{n\,n'}^{i\,i'}}{\partial R_l}a_{n',in}^{i'} + \frac{\partial T_{n\,n''}^{i\,i''}}{\partial R_l}W_{n''n'}^{i''\,i'}b_{n'}^{i'}\right)\right\} \quad (13)$$

In this way, we avoid explicitly calculating the derivatives $\frac{\partial \boldsymbol{b}}{\partial R_l}$, which require solving a separate system of equations for each individual partial derivative. Instead, we only solve one system of equations for the adjoint coefficients λ_n^i. This allows us to obtain the entire gradient by solving the forward system of equations given by equation (2) and the adjoint system of equations given by equation (12) just once.

Section S3. Optimization parameters

Table S2. Optimization parameters.

Wavelength	1.55 μm device	3 μm device
Initial radius	700 nm	1200 nm
Total spheres	3600	4900
Min, max radius	250, 1200 nm	250, 1400 nm
l_{max}, n_{max}	4, 48	3, 30
Periodicity	2.44 μm	2.9 μm
Device width	144 μm	200 μm
Initial, final FOM	2800, 0.095	4900, 1.9

Section S4. Mie coefficients

GMMT expands the initial and scattered fields in an infinite basis of SVWFs. However, for practical considerations, there is a suitable cutoff for the orbital angular momentum expansion l_{max} determined by the dimension and refractive index of the scatterer relative to the incident wavelength. This number corresponds to the maximum number of expansions n_{max} required to accurately characterize a scatterer using its corresponding Mie coefficients and is related to l_{max} by

$$n_{max} = 2l_{max}p(l_{max} + 2) \quad (14)$$

where p specifies the polarization. In general, scatterers with larger physical dimensions or refractive indices require higher expansion orders to accurately characterize. In our manuscript, the 1.55 μm device required a cutoff $l_{max} = 4$, while the 3 μm device required a cutoff $l_{max} = 3$. The justification of the choice of these parameters is shown in fig. S2, where we see that the maximum nonzero Mie coefficients for the 1.55 μm and 3 μm spheres are $l_{max} = 3$, and $l_{max} = 4$, respectively.

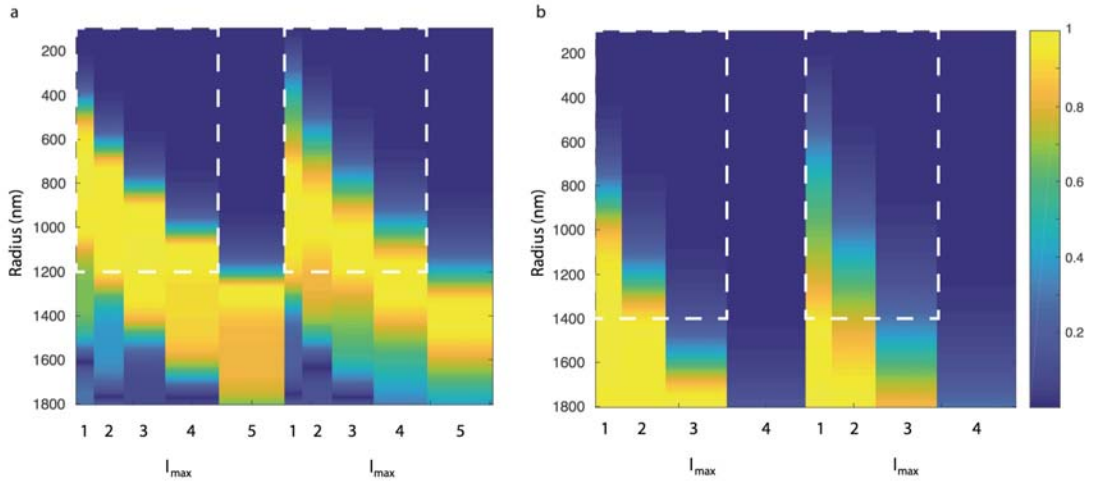

Fig. S2. Mie coefficients. Absolute value of the Mie coefficients for the sphere radii used in the device designed for (**a**) 1.55 μm and (**b**) 3 μm showing the validation of using the cutoffs.

Section S5. Effect of fabrication defects

In addition to the focal spots in Figures 2 and 3 from the main text of our final device, we present data from an initial device with more pronounced fabrication imperfections. An SEM of the device is shown in fig. S3, showing noticeably more fabrication imperfections. Here we can see that the experimental data in fig. S4 shows less contrast than Figure 2 in the main text, especially in the focal spots in the first three planes shown in fig. S3a-c. However, the focal spots are clearly discernible in fig. S3d-h. For the simulated spots, the focal spots are still clearly discernible from the background. To be able to compare the experimental and simulation results, we extract the positions of the simulated spots in an 80 μm × 80 μm window and use those positions as the center of an 8 μm × 8 μm window. In order to align the simulation and experimental images, we add an overall offset. Then, we search within the 8 μm × 8 μm window for the maximum, and call that our experimental maximum point. This data is used for fig. S6 showing the locations of the simulated maximums and also the experimental maximums.

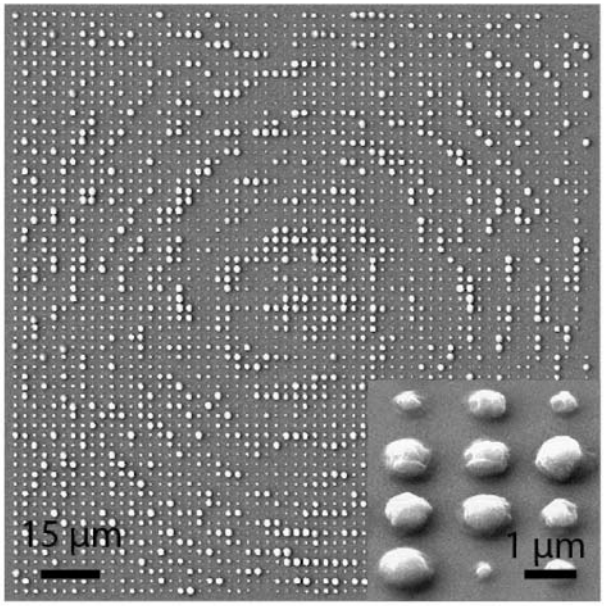

Fig. S3. SEM of the initial device. Top down view of entire device, with inset showing noticeable asymmetry in spherical scatterers.

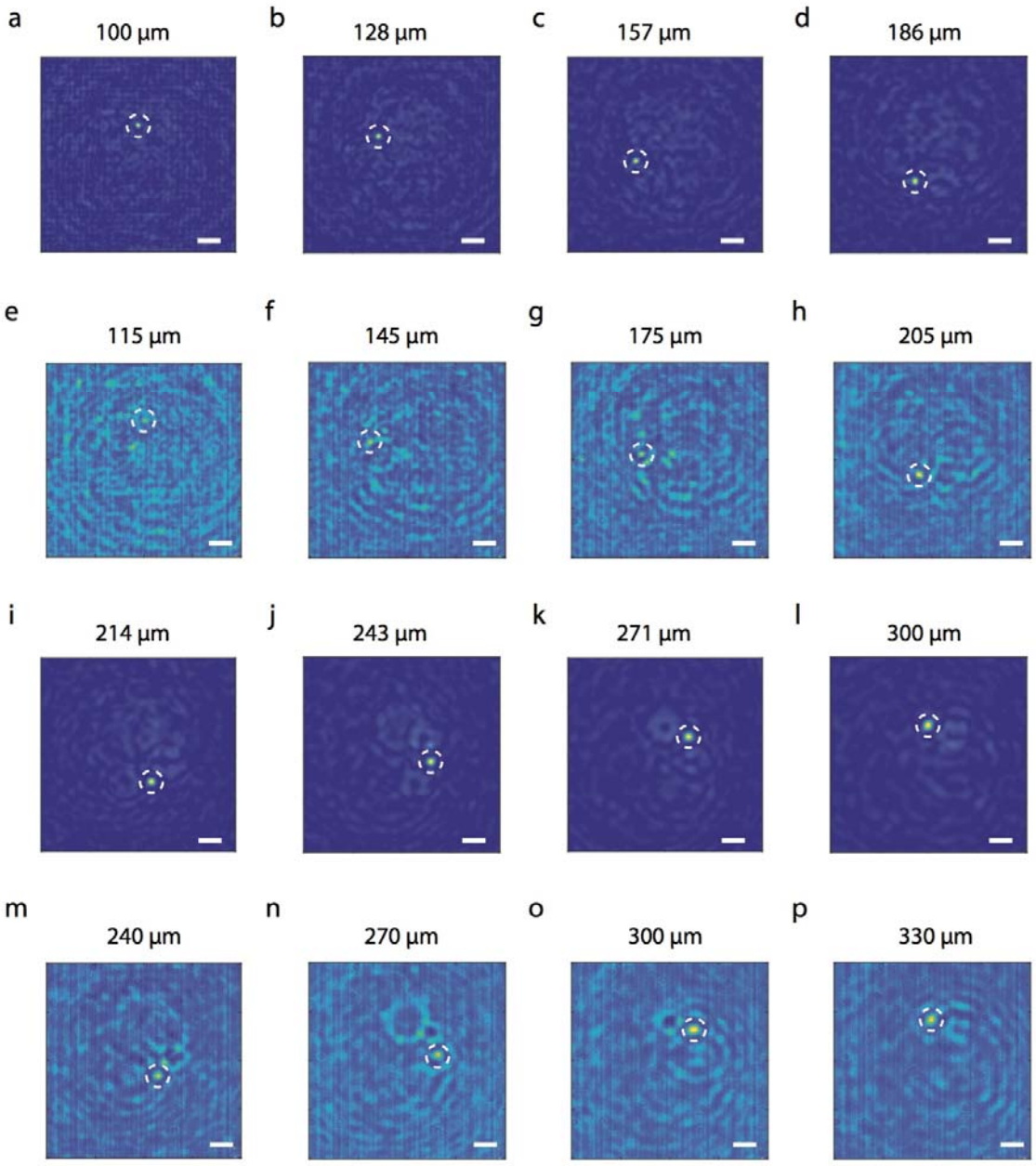

Fig. S4. Simulated and experimental device performance. (**a** to **d**), (**i** to **l**) simulated images of the intensity profile produced at specific distances from the device surface showing the focal spot rotating in the x-y plane. (**e** to **h**) and (**m** to **p**) Experimental images taken of the point spread function. Solid white scale bar is 10 µm.

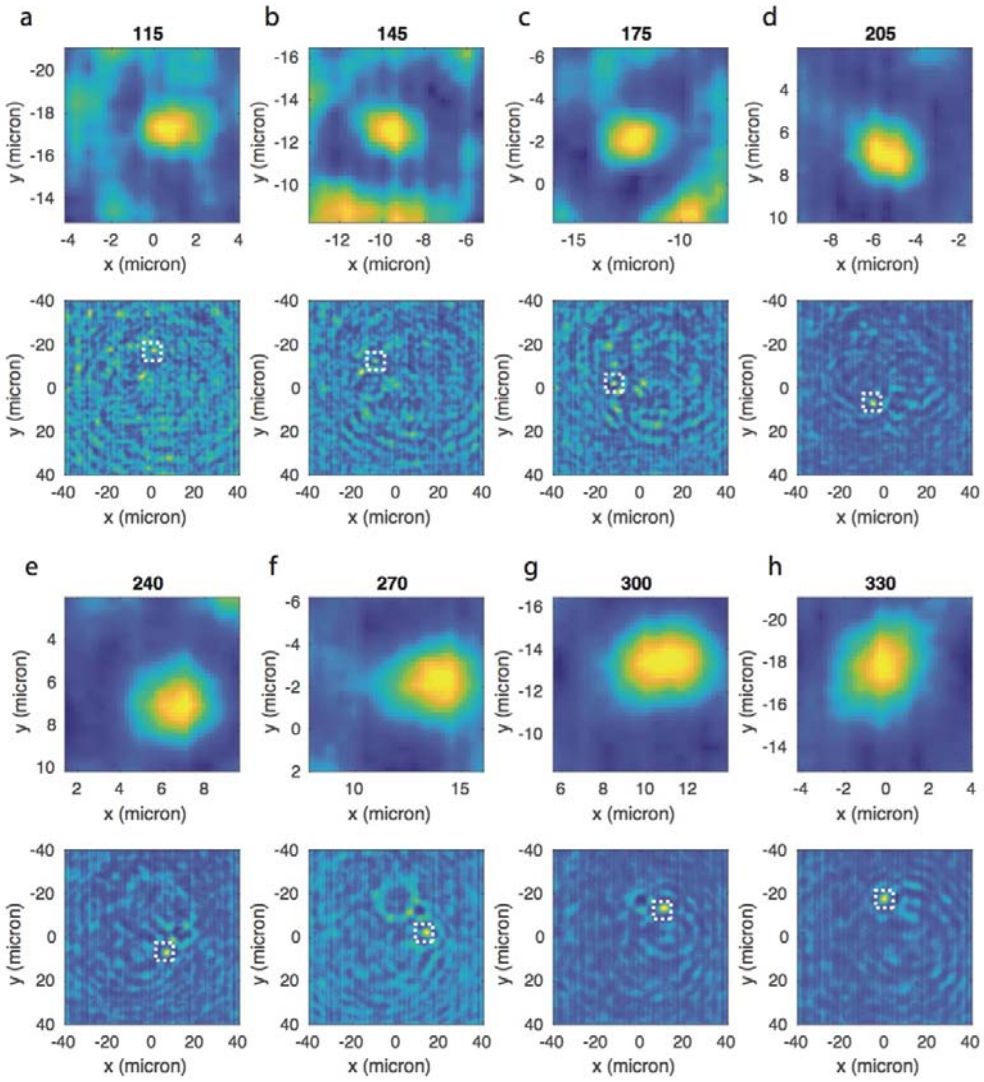

Fig. S5. Extracted focal spots and locations. (**a** to **h**) extracted focal spot profiles (top), and their locations in the x-y plane (bottom). The white dashed box has dimensions of 8 μm × 8 μm and represents where the focal spot profiles are.

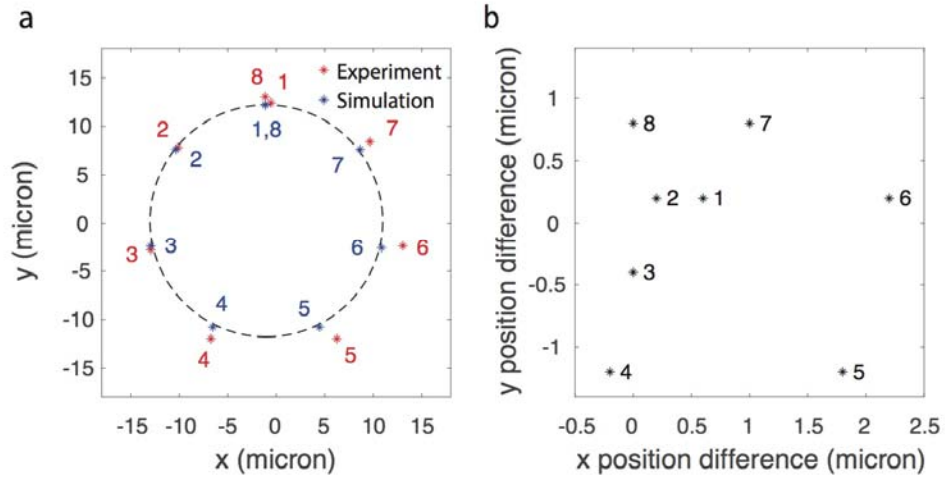

Fig. S6. In-plane focal spot comparison. (**a**) Focal spot locations of the experimental and simulated focal spots in red and blue, respectively. (**b**) Difference between expected location based on simulation and actual location of the focal spot in experiment.

Section S6. The 3 µm experimental and simulation data

The data from the device designed for 3 µm operation is presented below. With the simulation, and the experimental data in fig. S7. In simulation, the final device largely performed the designed functionality. When the simulated results are compared with the simulated results at 1.55 µm, the intensity profiles show more noticeable hot spots. The fabricated device in experiment performed relatively poorly. While there are focal spots that are identifiable producing a helical pattern, many of the simulated focal spots failed to appear, and also the contrast between the desired focal spot and other hot spots is low. We were not able to ascertain the correct locations of all of the spots in the experiment. The actual fabricated device is shown in fig. S8. The final device shows clear stitching issues due to the large field required to fabricate the device.

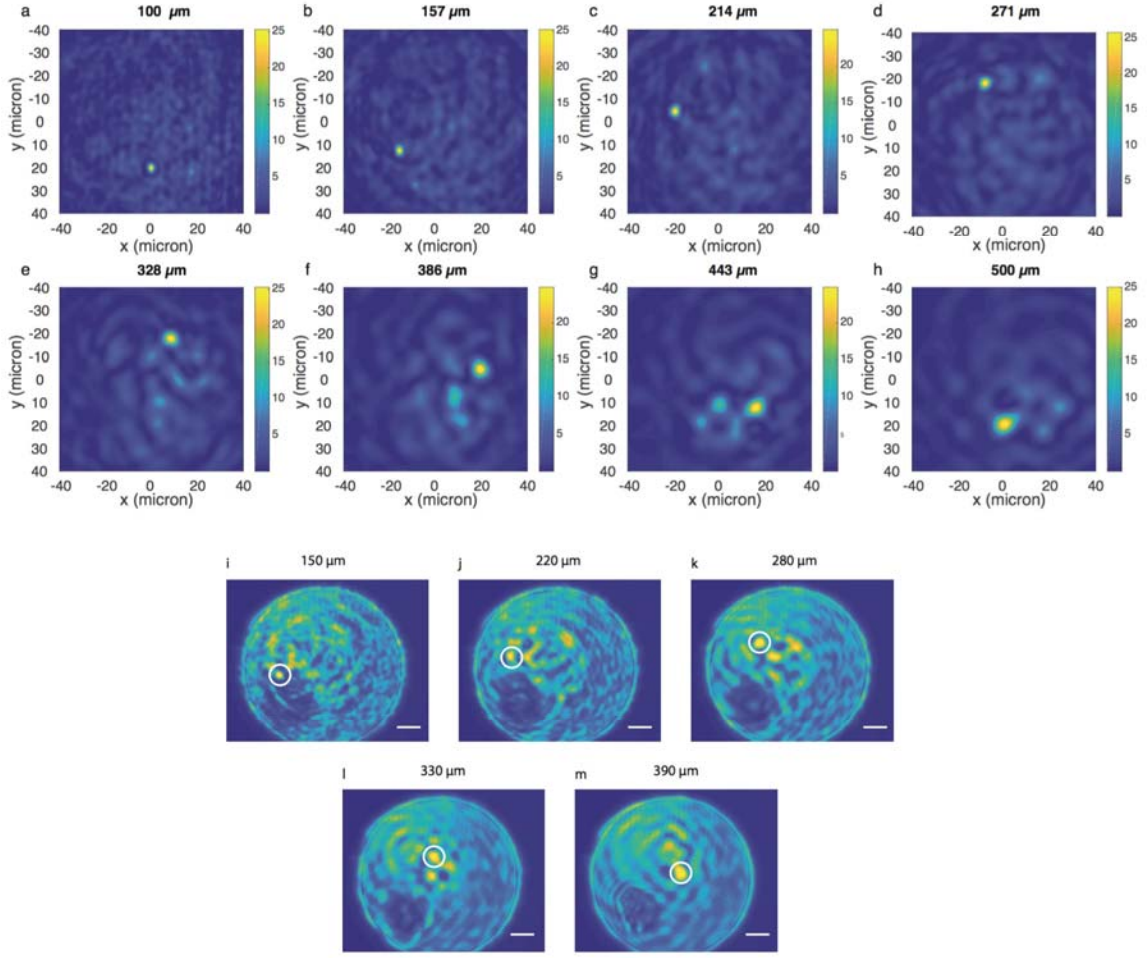

Fig. S7. The 3 µm simulated and experimental device performance. (**a** to **h**) Images of the intensity profile produced at specific distances from the device surface showing the focal spot rotating in the x-y plane. (i to **m**) five focal spots between 150-390 µm. White scale bar for (i to m) is 5 µm.

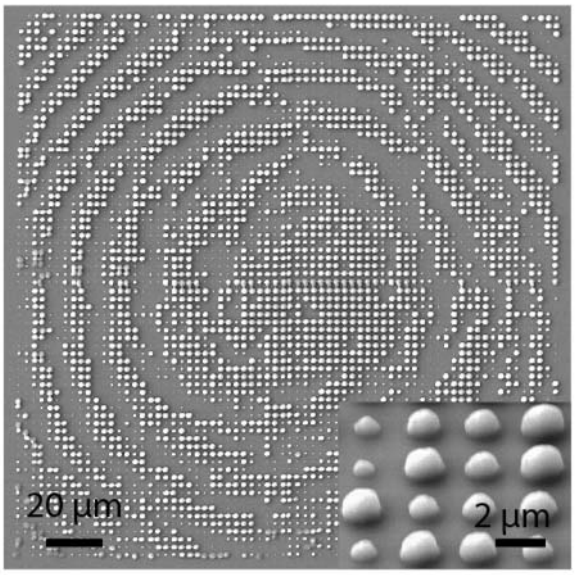

Fig. S8. The 3 µm device SEM. SEM of the fabricated 3 µm device showing some fabrication imperfection. Inset is a zoomed in view of the device.

Section S7. Computing resources

The inverse design method is described in detail in an earlier publication (*32*). The forward simulation method used is a branch of the freely available CELES software. The inverse design method is a custom extension of CELES that is available on request. The specifications of the hardware and software used in this paper are as follows:
AMD Ryzen Threadripper 1920x
Nvidia Titan Xp 12 GB
64 GB DDR4
CentOS 7
Matlab 2017b
CUDA 8.0
Both optimizations took approximately one day on this computer. For both optimizations, numerical zero was set to 0.001, which we found to be accurate enough for our simulations. The optimization process used LBFGS-B, and we chose BiCGSTAB as our numerical solver for both our forward and adjoint systems of equations.